This is the accepted manuscript made available via CHORUS. The article has been published as:

Surface adsorption and hopping cause probe-size-dependent microrheology of actin networks

Jun He and Jay X. Tang

Phys. Rev. E **83**, 041902 — Published 7 April 2011

DOI: 10.1103/PhysRevE.83.041902

Surface Adsorption and Hopping Cause Probe Size Dependent Microrheology of Actin Networks

Jun He and Jay X. Tang*

Department of Physics, Brown University, Rhode Island 02912, USA

Abstract

A network of filaments formed primarily by the abundant cytoskeletal protein actin gives animal cells their shape and elasticity. The rheological properties of reconstituted actin networks have been studied by tracking micron-sized probe beads embedded within the networks. We investigate how microrheology depends on surface properties of probe particles by varying the stickiness of their surface. For this purpose, we chose carboxylate polystyrene (PS) beads, silica beads, bovine serum albumin (BSA) coated PS beads, and polyethylene glycol (PEG) grafted PS beads, which show descending stickiness to actin filaments, characterized by confocal imaging and microrheology. Probe size dependence of microrheology is observed for all four types of beads. For the slippery PEG beads, particle tracking microrheology detects weaker networks using smaller beads, which tend to diffuse through the network by hopping from one confinement "cage" to another. This trend is reversed for the other three types of beads, for which microrheology measures stiffer networks for smaller beads due to physisorption of nearby filaments to the bead surface. We explain the probe size dependence with two simple models. We also evaluate depletion effect near non-adsorption bead surface using quantitative image analysis and discuss possible impact of depletion on microrheology. Analysis of these effects is necessary in order to accurately define the actin network rheology both *in vitro* and *in vivo*.

REVIEW COPY
NOT FOR DISTRIBUTION

*Electronic address: Jay_Tang@Brown.edu

I. Introduction

Despite the amazing diversity in size, shape and function of many eukaryotic cell types, nearly all of them consist of a prominent cytoskeleton formed from a network of protein filaments [1]. Understanding the mechanical properties of the cytoskeleton is crucial for assessing biological functions as diverse as cell motility, wound healing, organelle transport and phagocytosis. The predominant component of the cytoskeleton is a protein called actin, which assembles into filaments often referred to as F-actin. With a diameter of only 8 nm [2], actin filaments, or F-actin, are thin, but stiff, with a persistence length on the order of 10 micrometers [3, 4]. These rod-like filaments are of variable lengths and form highly compliant and deformable networks that are dynamically regulated in live cells, thereby performing their essential biological functions.

Because of the essential role of actin networks in cell mechanics, there has been extensive investigation of the rheological properties of actin networks reconstituted from pure actin [5–11], and in some cases with accessory actin binding proteins including those that crosslink actin filaments [12, 13], induce new branches [8], or cap filament ends to terminate their growth [14]. The results of these studies with reconstituted protein mixtures have reproduced in many aspects the viscoelasticity of live cells, and unraveled a number of intriguing mechanical properties of cells. For example, the typical elastic modulus of mammalian cells, on the order of 10^3 Pa [15], can be produced by crosslinked actin networks of as little as 1% protein content [16]. Additionally, the major features of a pre-stressed state, typical of live cells, have been mimicked by adding small aggregates of the actin motor protein myosin into the actin network [17, 18].

Over the past decade or so, particle tracking microrheology has been demonstrated as the most practical method for probing cell mechanics [17, 19–25]. Using micron- or submicron-sized probe particles, one can extract mechanical properties of materials the probes are embedded in, by measuring thermally driven motion [7, 19, 20, 26–30], or motion driven by an external force such as that generated by laser tweezers [31, 32] or magnetic tweezers [33, 34]. Since the probe size can be significantly smaller than the size of typical cells, local mechanical properties can be probed with sub-cellular resolution. Under certain situations, endogenous particles or self-assembled spots of labeled proteins naturally integrated into the networks of interest can be used as probes to acquire the viscoelastic properties of their

immediate environment [35].

It has been increasingly recognized that many factors complicate the interpretation of microrheology data. The most obvious limitation of single particle tracking is that probe particles unavoidably interact with the surrounding medium, thus reporting mechanical properties that have been altered by their presence. One method that has been shown to mitigate this local effect is to measure cross-correlations between two probe particles with a distance between them much larger than their own size [9, 22, 23, 36]. This two-particle method probes the properties of materials in the length scale longer than the distance between the particles, and is insensitive to short length scale properties and specific coupling between the probe and the medium [9, 36]. The two-particle microrheology measurements are shown to be more consistent with the bulk rheology results, though they almost ignore all the local microscopic properties. The actual cellular environment, however, is rich in structure and often renders the cross-correlation technique inapplicable. Therefore, the single particle method remains advantageous in probing cellular mechanics, since it is capable of reporting local properties in short length scale of the probe radius [37], usually not accessible by the two-particle method.

In this report, we address two commonly occurring factors that affect single particle microrheology: surface adsorption and hopping (illustrated in Fig. 1), both of which cause the measured rheological properties to be inaccurate and dependent on the probe size. Surface adsorption reduces the motion of micron sized probe beads, resulting in an artificial increase in measured stiffness [38, 39]. Hopping is the process by which small adsorption resistant probe particles hop over cages defined by the mesh size of the surrounding network. This hopping effect has been reported previously [9, 10]. In this paper, we focus on systematically characterizing probe size dependence of microrheology by varying surface coating and probe size, and correlate different trends of probe size dependence to different probe surface properties, characterized using quantitative confocal imaging. Two simple models are presented in order to assess size dependence. The expected outcome of this study is that undesirable effects, such as biased estimates of shear moduli and probe size dependence, may be eliminated by proper choice of the probe beads. Our work provides a simple guideline for optimization of probe surface chemistry and puts size dependent single bead microrheology data in proper context.

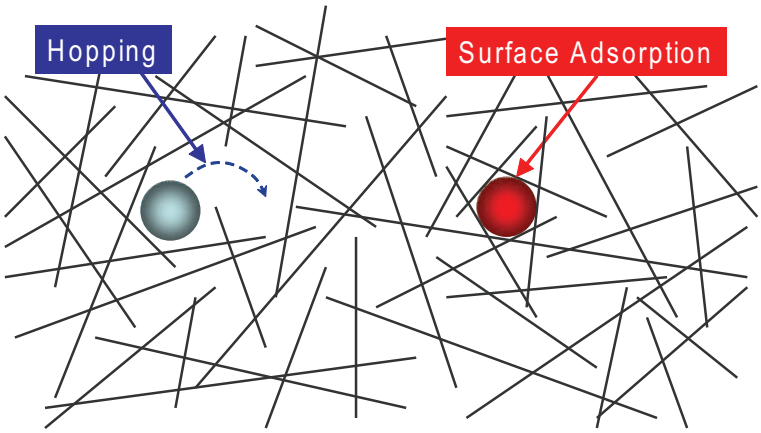

Figure 1: (Color online) A schematic illustration of two probe beads embedded in a network of actin filaments, showing two major effects producing probe size dependent microrheology. For the sticky bead (right), surface adsorption makes nearby filaments attach to the probe surface and increases the filament density near the surface of the bead. In the case of a slippery bead smaller than the network mesh size (left), the hopping effect dominates and the bead can hop from one confinement cage to another, thereby reporting an apparently weaker network.

II. Materials and Methods

Preparation of BSA coated PS beads

Rhodamine labeled bovine serum albumin (BSA) in dry powder form (Invitrogen Corporation, Carlsbad, CA) was dissolved in deionized water at a concentration of 2 mg/ml. Carboxylate polystyrene (PS) beads (Polysciences, Inc., Warrington, PA) with diameters of 0.45, 1.0, 2.0, 3.1 and 4.5 μm were added to 2 mg/ml Rhodamine BSA solutions in separate tubes and incubated at room temperature for 1 hour. A 20 mg/ml BSA stock solution was then added into each tube in excessive volume with which to incubate the beads for half an hour in order to further block open adsorption sites. The beads in suspension were then centrifuged at 6000 rpm for 5 minutes and the supernatants were discarded. Beads were resuspended with deionized water and then centrifuged again to the pellet. This wash process was repeated two more times. Prepared beads were kept in deionized water at 4 $^{\circ}C$ and used within one week of preparation. The same batch of beads were used for both microrheology measurements and confocal imaging.

Preparation of PEG grafted PS beads

To obtain the PEG coated PS beads, we followed the standard carbo-di-imide coupling chemistry used by Valentine *et al.* [39] to attach amine-terminated methoxy-poly(ethylene glycol), NH_2-$(CH_2$-CH_2-$O)_n$-OCH_3 (mPEG-NH_2), with average n=16 and average molecular mass of 750 Dalton (Rapp Polymere, Tübingen, Germany), to carboxylate PS microspheres. EDC (1-[3-(dimethylamino)propyl]-3-ethylcarbodiimide) (Sigma-Aldrich, St. Louis, MO) reacts with a carboxyl group to form an amine-reactive O-acylisourea intermediate, which is an unstable ester and will hydrolyze and regenerate the carboxyl group. With the presence of NHS (N-hydroxysuccinimide) at a lower pH, EDC converts carboxyl groups to the more stable amine-reactive NHS esters. The activated esters are then mixed with mPEG-NH_2 at a higher pH to react with the NHS-ester to yield a stable amide bond.

To avoid clustering of particles due to centrifugation or filtration, we followed a modified buffer exchange protocol using dialysis tubes as described in Ref. [39]. Microspheres (1 ml for each size) were loaded into dialysis tubes (SpectraPor, 10 kD cutoff; Spectrum, Rancho Dominguez, CA) at number densities of 10^{11}–10^{13} particles/ml; higher number densities result in aggregation and poor coupling efficiency. The bags were immersed in MES (100 mM 2-(N-morpholino)ethanesulfonic acid) buffer (100 mM MES at pH 6.0). Each step of dialysis or reaction was performed under constant gentle stirring. Then, the bags were submerged into MES buffer containing 75 mM EDC, 50 mM NHS, and a 200-fold excess of mPEG-NH_2 to carboxylate group for 1 hour to activate the reaction. The bags were then immersed into the borate reacting buffer (50 mM boric acid, 36 mM sodium tetraborate, 50 mM NHS, and 200 fold excess of mPEG-NH_2, pH 8.5) to allow the reaction to proceed for 8 hours. This step was repeated twice. After the reaction, the particles were washed with pure borate buffer (50 mM boric acid, 36 mM sodium tetraborate, pH 8.5) for 2 hours, twice, to remove unreacted reagents and polymer. Finally, the particles were recovered and stored in the pure borate buffer at 4 $^\circ C$, and were used over several months.

Preparation of actin and Alexa-488 labeled actin for confocal imaging

Actin was extracted from rabbit skeletal muscle following the technique of Pardee and Spudich [40]. The extracted actin, kept in G-buffer (2 mM Tris-HCl, pH 8.0, 0.5 mM ATP,

0.2 mM $CaCl_2$, 0.5 mM DTT, and 0.005% sodium azide), was frozen with liquid nitrogen and stored at $-80\ ^{\circ}C$. Fluorescently labeled G-actin used for confocal imaging was prepared following the procedure described by Kuo and Fisher [41]. G-actin was labeled on a random amino acid group using Alexa 488-succinimidyl ester (Invitrogen Corporation, Carlsbad, CA). G-actin was dialyzed against P-buffer (50 mM PIPES, pH 6.8, with 50 mM KCl, 0.2 mM $CaCl_2$, and 0.2 mM ATP) to polymerize while removing the interfering Tris present in the actin buffer. Alexa 488-succinimidyl ester (30 mM), dissolved in dimethyl formamide, was added drop-wise to a 7.5-fold molar excess over actin (typically 60 μM). After incubation for one hour at room temperature in the dark, the reaction was quenched by adding 20 mM Tris, pH 8.0, 16 mM ATP, 10 mM K-glutamate, 5 mM lysine, and 5 mM DTT, followed by dialysis against the buffer (2 mM Tris, pH 8.0, with 0.2 mM ATP, 0.5 mM DTT, 0.25 mM $CaCl_2$, 0.05 mM EDTA, and 0.05% sodium azide). Using a spectrophotometer to determine the labeling efficiently with manufacturer's extinction coefficient, we found the labeling to be sub-stoichiometric, of typically 0.42-0.5 dye molecule per actin monomer. Polymerization of the actin partially labelled using this protocol yielded fluorescent actin filaments of smooth, semiflexible appearance, averaging several micrometers in length. We conclude that this labeling process did not adversely affect the protein. For storage, the Alexa 488 labeled actin was stored frozen in 10% sucrose (w/v) at -80°C. On the day of experiment, an aliquot of the labeled actin was thawed rapidly in waterbath to 25 $^{\circ}C$ and centrifuged for 5 min at 7000 g to remove debris. The G-actin was polymerized to form F-actin by adding the salts KCl and $MgCl_2$ to the final concentrations of 50 mM and 2 mM, respectively. For this study, we used the partially labeled protein from a single batch of preparation to make samples for confocal imaging, as well as for microrheology. The average filament length of F-actin polyerized from this batch of labeled actin was detected to be approximately 7 μm under the specified polymerization condition.

Confocal imaging of beads and actin network

The visualization of the actin network embedded with probe beads, including the Rhodamine BSA coated beads, was performed with a Leica confocal Laser scanning microscope, using a 100x oil immersion lens. The images taken were in 512×512 pixels, covering a $49.7 \times 49.7\,\mu m$ region (with pixel size $0.097 \mu m$). Alexa-488 labeled actin was excited by an

argon laser (wavelength 488 nm) and the Rhodamine BSA was excited by a helium-neon green laser (wavelength 543 nm). The samples for confocal imaging were filled between a coverslip and glass slide, sealed with vacuum grease. The sample thickness was between 20 and 25 μm. The images of beads and actin network were acquired at the equator of each selected bead using corresponding excitation lasers, while keeping the field of view fixed.

Extracting azimuthally averaged intensity profile of confocal bead image

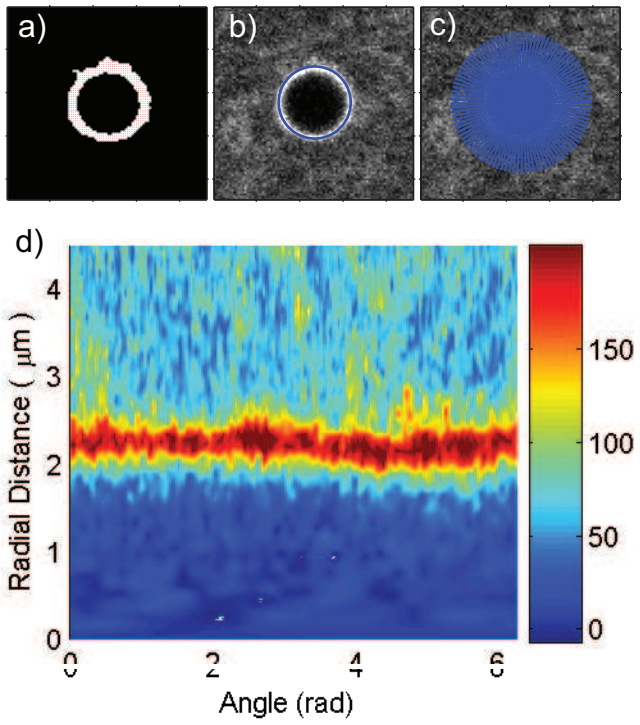

Figure 2: (Color online) Azimuthally unwrapped intensity profile. (a) The equator plane of a bead confocal image is thresholded to become a binary image. (b) Bright pixel positions are fitted to a circle with the MatLab least square distance method to determine the bead center. (c) A polar meshgrid is applied on the bead image centered at bead center with fluorescence intensities bilinearly interpolated at each grid node. (d) Interpolated intensities on the polar meshgrid are plotted on a color map as a function of radial distance and azimuthal angle. The circular geometry is unwrapped to a linear geometry, and azimuthal angles can be averaged out to obtain an averaged intensity profile shown in Fig. 3c-d as a function of radial distance.

Azimuthally averaged intensity profile of confocal bead image is used to determine surface affinity of different bead coatings, or to measure the depletion layer thickness. The average intensity profile is obtained according to the following steps using MatLab (Mathworks, Natick, MA). First, confocal images of beads (either BSA coating or beads embedded in

labeled F-actin solution) are thresholded to become a binary image of a ring (Fig. 2a): the threshold value is chosen to be the mean image intensity plus 0.5 times of the standard deviation of the image, and pixels with intensity larger than a threshold value are set to be one, the rest zero. Then, the pixel coordinates are fitted with a circle using the MatLab function "lsqnonlin", which implements a nonlinear least square fit, in this case to minimize the sum of squared distances of the pixel positions from the circle (Fig. 2b). Fitting to a circle yields a center coordinate and radius, and the fitting uncertainty of the circle center is below 1/10 of pixel size. Next, a polar coordinate grid is applied on the bead image centered at the fitted bead center to bilinearly interpolate the intensity at every grid node (Fig. 2c). The radial spacing of the polar grid is 0.1 pixel size and the angular spacing of the polar grid is 0.5 pixel size divided by the circle radius. The radial intensity is highly over-sampled to obtain high radial resolution. The final result is a re-interpolated intensity profile of beads un-wrapped in Cartesian coordinates of radial distance and angle (Fig. 2d). Averaging out the angles yields the azimuthally averaged intensity profile as a function of radial distance (Fig. 3e-h).

Sample preparation for microrheology

Probe beads used in the microrheology measurements include carboxylate PS beads (Polysciences Inc., Warrington, PA), silica beads (Bangs Laboratories, Inc., Fishers, IN), BSA coated PS beads and PEG grafted PS beads, prepared as described above. Diameters of the PS beads and those derived from them are 0.45, 1.0, 2.0, 3.1 and 4.5 μm; diameters of silica beads are 0.32, 0.57, 1.0, 2.0, 3.0 and 4.5 μm. The standard deviations of bead diameters are 0.5-2% as specified by the vendor, and our measurements of those of larger sizes by confocal imaging confirm the vendor's specification. The effect of coating of either BSA or PEG on the size of PS beads is negligible since both molecules are within a few nanometers in size. Beads were diluted with actin buffer and then mixed with a polymerized actin solution and allowed sufficient time to be incorporated and equilibrated into the actin network. Note in this report we address all test samples interchangeably as "F-actin solution" or "actin network", bearing in mind that the long and semiflexible actin filaments form an entangled network under the test conditions.

To avoid systematic errors due to sample-sample variation, all the beads with different

sizes were mixed in the same F-actin solution and measured in the same sample. The beads were manually picked and each compared with template bead images to determine their size. This practice prevented us from automation of multiple bead tracking in one field of view, thus the number of beads measured for each size was limited to about 30. To compensate for this limitation and to obtain averaged low frequency motion, large data samples of 10000 frames of images were acquired. The long measurement time made it crucial that there be no residual flow in the sample and no drift of the microscope stage. To achieve that, the sample was injected into rectangular glass capillaries with cross-sectional dimensions of $0.1\,\mathrm{mm} \times 1\,\mathrm{mm}$ (VitroCom Inc., Mt. Lakes, NJ) for convenient microscopic observation. The filled capillary was sealed with an inert glue to eliminate flow and evaporation. In assessment of the measurement reliability, each MSD curve was obtained as average of those from at least 10 beads, and error bars show the variation of those beads of the same size within the same sample.

Video particle tracking microrheology

To implement the Video Particle Tracking (VPT) method, we first track the motion of beads embedded in the material of interest using a Nikon E800 upright microscope equipped with a Cool-Snap HQ CCD camera (Photometrics, Tucson, AZ). Time-lapse videos of beads were taken using a 100x objective in the middle of the capillary cavity so that the beads were far away from the glass walls or any air-liquid interface. The positions of centroids of beads were extracted from the video using the thresholding algorithm in Metamorph 6.0 (Universal Imaging Corp., Downingtown, PA), which has a tracking resolution smaller than one pixel (0.0645 μm).

The ensemble averaged mean square displacement (MSD), $\langle \Delta r^2(t) \rangle$, is calculated from the bead positions. The complex shear modulus $G^*(\omega)$ is related to the Fourier transform of $\langle \Delta r^2(t) \rangle$ through the generalized Stokes-Einstein (GSE) relation [19, 42]:

$$G^*(\omega) = \frac{k_B T}{\pi R_0 i\omega \mathcal{F}\left\{\langle \Delta r^2(t) \rangle\right\}}\,, \tag{1}$$

where k_B is the Boltzmann constant, T is the absolute temperature, R_0 is the bead radius, ω is the angular frequency, i is the imaginary unit and $\mathcal{F}$ represents Fourier transform.

This equation has been derived by Mason *et al.* [19], assuming a sphere with negligible mass embedded in an incompressible and isotropically viscoelastic medium with a no-slip boundary condition. To overcome the truncation errors of Fourier transform near the two frequency extremes, we use the method developed by Mason *et al.* [43] to estimate the transforms algebraically by applying a local power law expansion around a frequency of interest ω, and retaining the leading term, which yields the frequency dependence of the storage modulus $G'(\omega)$ and the loss modulus $G''(\omega)$,

$$G'(\omega) = |G^*(\omega)| \cos(\pi\alpha(\omega)/2)\,, \tag{2}$$

$$G''(\omega) = |G^*(\omega)| \sin(\pi\alpha(\omega)/2)\,, \tag{3}$$

where $\alpha(\omega) \equiv \frac{\mathrm{d}\ln\left\langle\Delta r^2(t)\right\rangle}{\mathrm{d}\ln t}\Big|_{t=1/\omega}$ and $|G^*(\omega)| = k_BT/\left\{\pi R_0 \left\langle\Delta r^2(1/\omega)\right\rangle [\Gamma(1+\alpha(\omega))]\right\}$. Here $\Gamma(1+\alpha(\omega))$ is the Gamma function with a complex functional form.

Curve fitting, statistical tests

Curve fitting is performed using the "nlinfit" function in MatLab, which implements a least squares fit with the Levenberg-Marquardt algorithm. The parameter standard deviations are calculated from the square roots of diagonal elements of the covariance matrix output from "nlinfit". The p-values of Student's t-test performed for the measured depletion layer thickness are computed using the MatLab function "ttest". Student's t-test performed for whether the fitted scaling exponents significantly differ from -1 follows the standard procedure of hypothesis testing. The t statistics are calculated as the ratio of parameter estimate to parameter standard deviation (both output from MatLab), and the p-value is obtained using cumulative probability function of t-distribution supplied by MatLab.

III. Results

Direct comparison of protein adsorption by confocal imaging

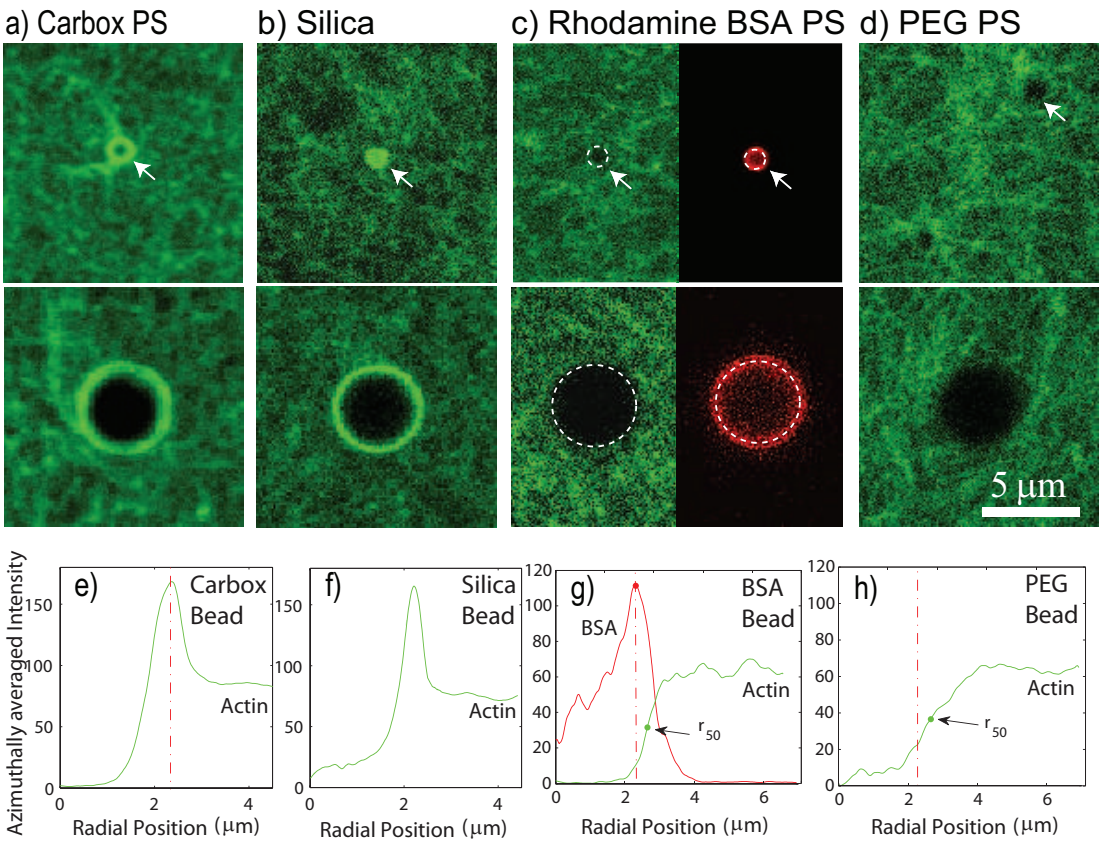

Figure 3: (Color online) Confocal images of Alexa-488 labeled F-actin solutions (0.34 mg/ml) embedded with beads of different surface properties visualized at the bead equator section. Four types of beads are shown: (a) carboxylate PS beads, (b) silica beads, (c) Rhodamine BSA coated PS beads, and (d) PEG grafted PS beads, all with 1 μm beads shown in the top row and 4.5 μm beads shown in the bottom row. The white arrows indicate the locations of the 1 μm beads. A scale bar of 5 μm, shown at the lower right corner, applies to all the images. For (c), Rhodamine BSA coated PS beads, BSA coating is also shown on the right with TRITC fluorescence. The circles in white dashes in (c) are obtained from the center threads of the bright fluorescence rings of BSA beads, intended to show the boundaries of BSA coated beads. (e)-(h) Azimuthally averaged intensity profile of actin (green) and BSA (red) for corresponding 4.5 μm beads shown in (a)-(d). BSA profile in (g) is plotted to show bead boundary. Red dash dot lines in (e), (g) and (h) show the boundaries of PS bead identified by the BSA profile. In (g) and (h), the green dots show the 50% intensity point on actin profiles. The differences of the radial positions between the red lines and the green dots are identified as the depletion layer thickness.

Protein filaments such as F-actin tend to physisorb on the surface of many types of probe beads [38, 39]. Before addressing this surface adsorption effect on microrheology, we first

compared fluorescently labeled F-actin networks near embedded test beads with four types of surface properties using a confocal microscope. Figure 3 compares representative images of these four types of beads at equator planes, all embedded within the 0.34 mg/ml actin network. Rhodamine labeled BSA was used to coat the PS beads, so that the surface of the BSA beads could be determined by the red fluorescence profile. The enhanced green fluorescence on the surfaces of carboxylate PS beads and silica beads is due to the adsorbed actin filaments, with the former showing slightly brighter and thicker rings indicative of stronger adsorption. There is no visible actin adsorption on the BSA and PEG beads, and the difference between them in actin coating, if any, is hard to detect by confocal imaging. To quantify the surface affinity of different bead surfaces, we convert the two dimensional intensity field of probe beads in F-actin solution into azimuthally averaged intensity profile (see method section for details). Figure 3e-h show the azimuthally averaged intensity as a function of radial distance from the respective centers of four types of beads in Fig. 3a-d. We use two metrics to compare the surface affinity: one is the ratio of maximal peak value of azimuthally averaged intensity to the background solution intensity $R_{max,bkgd}$, and the other is the ratio of integrated intensity of the peak to the mean background solution intensity $R_{peak,bkgd}$. (A peak is defined as part of the curve where the intensity values are above the maximum of azimuthally averaged background intensity.) $R_{max,bkgd}$ is dimensionless, but $R_{peak,bkgd}$ has a unit of length. The two quantities are both calculated for over 30 carboxylate or silica beads, and the mean values are shown in Table I along with the standard deviations. For the carboxylate beads, $R_{max,bkgd}$ and $R_{peak,bkgd}$ are approximately 10% and 7% higher, respectively, suggesting that they have slightly stronger absorption of actin filaments than the silica beads. For beads with non-adsorption surface such as the BSA and PEG beads, such analysis can not be applied. Instead, we conduct a similar analysis to measure depletion layer thickness for these two types of beads, the results of which are detailed below.

Bead type	$R_{max,bkgd}$	$R_{peak,bkgd}$ (μm)	Depletion thickness (μm)/p-value	Adsorption	Depletion effect
carbox PS	2.21±0.20	1.17± 0.29	N/A	strongest	no
silica	2.02±0.07	1.10±0.08	N/A	strong	no
BSA PS	N/A	N/A	$0.27 \pm 0.07 / 1.1 \times 10^{-5}$	weak	yes
PEG PS	N/A	N/A	$0.29 \pm 0.04 / 1.97 \times 10^{-7}$	no	yes

Table I: Summary of analysis results for bead surface adsorption and depletion. Listed parameters include surface adsorption $R_{max,bkgd}$ and $R_{peak,bkgd}$, and measured depletion layer thickness and their corresponding p-values. Rankings of adsorption and depletion are also listed.

Depletion effect of probe particle detected by confocal imaging

The depletion effect, in which stiff or semiflexible filamentous polymers are prevented from penetrating a hard surface, is known to create a less dense network near probe surface, thereby affecting the results of particle tracking microrheology [44]. Such an effect for the case of micron sized beads in actin network has been probed by diffusing wave spectroscopy [45, 46]. A more direct measurement of depletion layer has recently been made between actin networks and a BSA coated flat glass surface using confocal microscopy [41]. Fisher and Kuo defined the depletion layer thickness as the distance from the peak position of fluorescence profile of the BSA surface coating to the half maximum position of actin fluorescence intensity. For spherical beads, we interpolate the fluorescence intensity at different angles along radial distance from the center of beads, and un-wrap the intensity profile to form a flat surface (Fig. 2d, see method section for details). With this mapping, the depletion layer may be determined in the same way for spherical probe particles as performed for a flat glass surface. The radial profiles in different angles should be the same, hence we average out the angles and obtain the azimuthally averaged intensity profile. We define the depletion layer thickness to be the distance from the peak position of the fluorescent BSA coating, r_{peak} (red dot in Fig. 3g and h), to the half drop position of actin fluorescence from the bulk towards the bead center, r_{50} (green dot in Fig. 3g and h). We measured the depletion layer thickness, $r_{50} - r_{peak}$, for 10 BSA coated beads and 10 PEG grafted beads all 4.5 μm in diameter. We use the same mean r_{peak} of BSA coated beads for PEG grafted bead, since they are both made from the 4.5 μm carboxylate PS beads and the change in radius caused by either coating is estimated to be within a few nanometers. The mean and

standard deviation of depletion layer thickness for BSA beads and PEG beads are measured to be 0.27 ± 0.07 and 0.29 ± 0.04 μm, respectively (summarized in Table I). The standard deviations show the variation across different beads. The depletion layer thickness measured for the BSA beads is slightly smaller than that for the PEG beads, but this difference is statistically insignificant. Note that the measured depletion layer thickness is about 3 pixels of the confocal images (pixel size ~ 0.097 μm). We performed a two tailed Student's t-test, and obtained the p-values to be 1.1×10^{-5} and 1.97×10^{-7} for the BSA and PEG beads, respectively. Both p-values are well below the standard criterion for significance, 0.05, to reject the null hypothesis that the mean is zero, thus proving the existence of non-zero depletion thickness. For smaller beads, however, complications due to sharp surface curvature and smeared signal from labeled proteins out of the focal plane rendered the measured depletion layer thickness unreliably small. As a result, our method is not sensitive enough to resolve the depletion layer thickness of smaller beads, thus unable to correlate the probe size dependency with the depletion layer thickness.

In summary, based on the azimuthally averaged intensity profile analysis of confocal bead images, carboxylate PS, silica, and BSA/PEG beads rank from strong to weak in surface adsorption. The order between the BSA and PEG beads cannot be determined by the confocal images alone, but it is later determined by micro-rheology that PEG beads are the least absorbing. Approximately the same thickness of depletion layer was observed for BSA and PEG treated beads, whereas the depletion effect was totally masked by adsorption for the other two bead types (summarized in Table I).

Probe surface property leads to size dependent viscoelasticity

To assess the effect of surface properties on network mechanics, we performed single particle tracking measurements using the four types of beads. Figure 4a shows a representative MSD plot of different sized BSA coated PS beads in 0.34 mg/ml F-actin solutions. The MSD data for BSA beads show, for instance, that smaller beads displayed larger MSDs (Fig. 4a), consistent with the GSE relation. The GSE relation predicts the MSD to be inversely proportional to the radius of probe beads. Equivalently, the scaled MSD (MSD times probe radius) is expected to be the same for different probe size, and the resultant moduli should not depend on probe size. Yet, upon close inspection, the scaled MSDs of

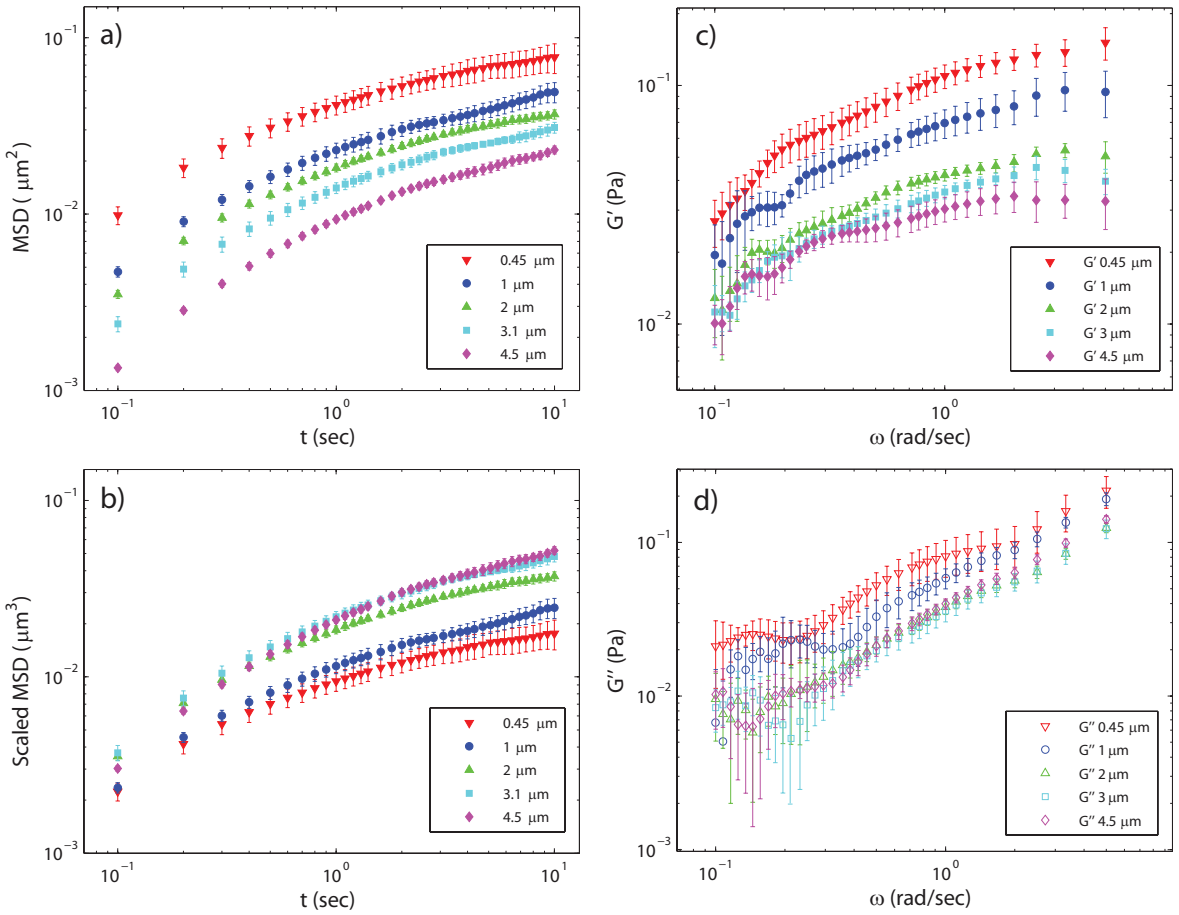

Figure 4: (Color online) MSDs of BSA coated PS beads embedded in F-actin solutions and the corresponding shear moduli spectra. (a) and (b): MSDs and scaled MSDs (MSD$\times R_0$) as functions of lag time are plotted for different sized BSA coated PS beads in a 0.34 mg/ml F-actin solution. All the beads with different sizes are measured in the same F-actin solution to eliminate sample-sample variation, and 10000 frames of images are acquired for each beads at the sampling time interval of 0.1 seconds. Each MSD curve is an average of MSD curves of 10 individual beads, and error bars show variation of MSD curves of different beads. (c) and (d): The frequency spectra of storage and loss moduli are shown for a 0.34 mg/ml F-actin solution measured with BSA coated PS beads. Spectra are converted from MSD data shown in (a) using Eq. 2 and 3.

BSA beads do not collapse but rather they increase slightly with bead size, suggesting a residual dependence on the probe size (Fig. 4b). Similar probe size dependence is observed for the other two types of sticky beads, carboxylate PS and silica. which will be addressed later. After the MSD data were Fourier transformed to yield the storage and loss moduli G' and G" through the GSE relation, both values appeared to be higher when probed by smaller beads over the entire frequency range for BSA beads (Fig. 4c and d). The same is true for the two types of sticky beads. Even though BSA coated beads are traditionally

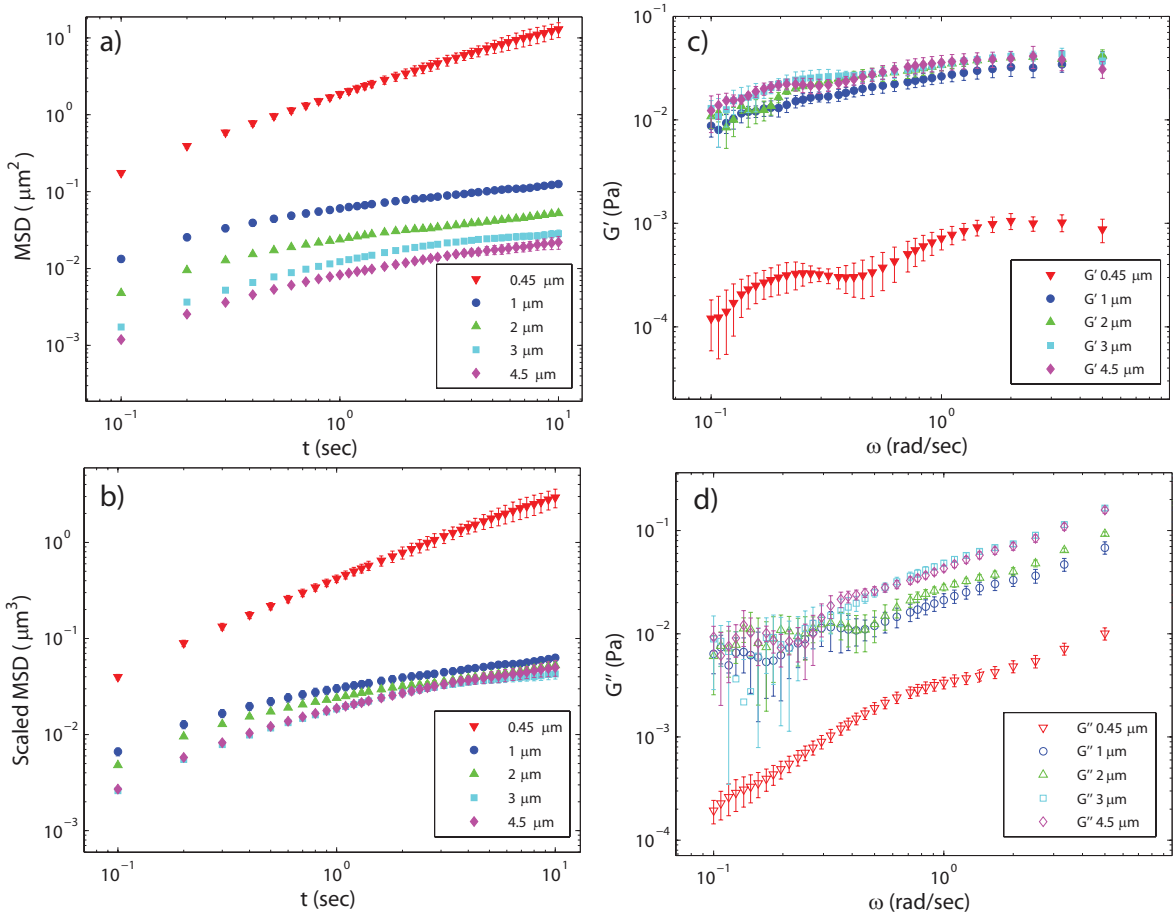

Figure 5: (Color online) MSDs of PEG coated PS beads embedded in F-actin solutions and the corresponding shear moduli spectra. (a) and (b): The MSDs and scaled MSDs of PEG coated PS beads in 0.34 mg/ml F-actin solutions as functions of lag time, plotted for five different bead diameters. Error bars show variation of MSDs of different beads, and the same imaging condition was used as the BSA beads. (c) and (d): The frequency spectra of storage and loss moduli measured by PEG beads, converted from the MSD data shown in (a).

considered non-sticky [38], they show similar size dependence as the two stickier types of beads.

Cage hopping detected using adsorption resistant beads smaller than the network mesh size

Contrary to the other three bead types, the PEG functionalized PS beads prove to be adsorption resistant. Figure 5 a and b show a much larger MSD and scaled MSD of 0.45 μm PEG beads than the bigger beads in 0.34 mg/ml F-actin solutions. This is because at this protein concentration, the 0.45 μm PEG-beads are smaller than the network mesh

size, which is estimated to be about 0.51 μm [47]. Therefore, these small beads may move through the network by hopping. The larger beads are progressively more constrained by the surrounding actin network, showing smaller MSDs (Fig. 5a). Figure 5b shows the scaled MSDs of PEG beads to decrease with the bead diameter, a probe size dependent behavior opposite to that of the BSA beads, especially for diameters between 0.45 and 1.0 μm. The dominant cause for the probe size dependence of PEG beads ought be the cage hopping effect, because bigger beads have less chances to hop. This dependence may not be attributed to the depletion effect, which is expected to affect the PEG beads similarly to the BSA beads, but the opposite dependence is found for the later. When MSDs are translated into shear moduli, both G' and G'' increase with the bead diameter across the entire frequency range when probed by PEG coated beads, but the increase with the bead size appears rather weak with the exception for the 0.45 μm PEG beads. The smallest beads detect significantly smaller moduli, for they were able to "hop" through the network (strictly speaking, they do not really report the moduli of the network). Thus, for the adsorption resistant slippery probes, smaller beads probe an apparently softer network due to the cage hopping effect.

The cage hopping effect was first reported by Gardel *et al.* [9]. They used carboxylate PS beads incubated with G-actin solution before actin polymerization, which we expect to behave similarly to BSA coated beads. In our experiments, however, the hopping phenomenon was not observed for BSA coated beads, perhaps suggesting that a small number of open adsorption sites on BSA coated beads make them slightly sticky and adhere to actin filaments. This marked difference implies that the coating of PS beads by monomeric actin prior to polymerization in their study might have blocked the adsorption of actin filaments more thoroughly than that of BSA used in our experiments. Mixing beads with G-actin before its polymerization led to the observation of the hopping effect in the earlier work, although this important point was not stressed in their publication [9]. We missed using this trick during our experiments, but the different outcome in this study leads to better appreciation of how strong the surface adhesion effect is on particle probe micro-rheology.

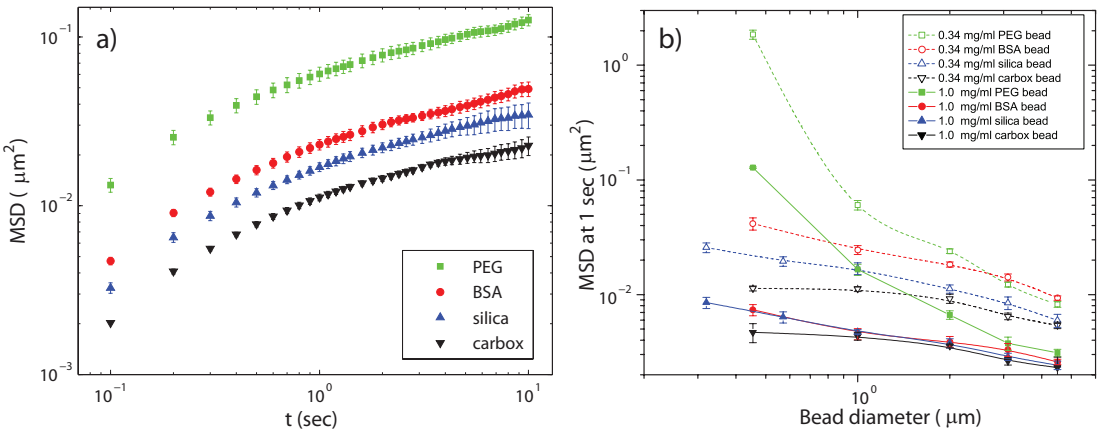

Figure 6: (Color online) (a) MSDs as functions of lag time plotted for four types of 1 μm beads embedded in 0.34 mg/ml F-actin solutions. (b) MSDs at 1 sec plotted as functions of bead diameter for two F-actin concentrations, 0.34 mg/ml (dash lines) and 1.0 mg/ml (solid lines). Carboxylate PS beads are in inverted triangles, silica beads in blue triangles, BSA PS beads in circles, and PEG PS beads in squares. The MSD were adopted at 1 sec lag time from MSD curves as shown in Fig. 4a and Fig. 5a. Error bars show the variation of MSD of different beads with the same diameter.

Statistical significance of probe size dependent microrheology

Probe size dependent microrheology is manifested as MSD scales with probe diameter with an exponent not equal -1. Figure 6a shows MSD vs lag time for different types of 1 μm beads embedded in 0.34 mg/ml F-actin solutions. In the order of carboxylate PS beads, silica beads, BSA coated carboxylate PS beads, and PEG grafted beads, we note an increasing average motion (MSD) of the probe beads, corresponding to decreasing stickiness. Figure 6b summarizes the MSD at 1 second lag time as a function of bead diameter for all four types of beads, and the scaling exponents are obtained from fitting the curves to a power law function with results summarized in Table II.

The uncertainty involved in microrheology measurements is typically large (about 8 to 20% variation in MSDs among different beads for our case). Thus, one might speculate that this probe size dependency could be mainly attributed to measurement errors. We prove here, however, that this probe size dependency is statistically significant. We perform a Student's t-test for the power law regression exponent, where the scaling exponent of -1 is the null hypothesis (see methods section for details). MSD at 1 second vs. bead diameter curves are fitted to a power law function using the MatLab "nlinfit" function. (Best fitting lines are not plotted, and 0.45 μm PEG beads are not included in the fitting.) The fitting results for eight different curves are summarized in Table II. Surface properties characterized

C_a (mg/ml)	Bead type	Mean exponent	St. dev.	T statistics	P-value	Surface properties
0.34	PEG	-1.36	0.029	12.29	0.0033	no adsorption/notable depletion
0.34	BSA	-0.60	0.036	11.38	0.0007	weak adsorption/notable depletion
0.34	silica	-0.48	0.040	12.99	0.0001	strong adsorption
0.34	carboxylate	-0.28	0.082	8.74	0.0016	stronger adsorption
1.0	PEG	-1.30	0.014	21.29	0.0011	no adsorption/notable depletion
1.0	BSA	-0.44	0.044	12.68	0.0005	weak adsorption/notable depletion
1.0	silica	-0.46	0.025	21.53	0.0001	strong adsorption
1.0	carboxylate	-0.29	0.058	12.29	0.0006	stronger adsorption

Table II: Summary of the power law fitting and Student's t-test results for eight different MSD vs. bead diameter curves (four different probe types and two actin concentrations) in Fig. 6. The parameters compared include the mean exponents, the standard deviations given by nonlinear fit, the T statistics, and the corresponding p-values. The last column lists the surface properties characterized by quantitative confocal imaging.

by confocal image analysis are also shown in the last column. Table II shows that the mean scaling exponent is smaller than -1 for slippery beads, and larger than -1 for sticky beads. The p-values of the two tailed Student's t-tests are between 0.0001 and 0.005 for all curves, way below the typical requirement of 0.05 to reject the null hypothesis, proving that the probe size dependency is statistically significant.

Opposite trends of probe size dependence of moduli for adsorption and non-adsorption probes

Figure 7 summarizes the shear moduli measured at 1 rad/sec as functions of bead diameter for all four types of beads. This comparison shows opposite trends of probe size dependence of moduli measured by the adsorption and non-adsorption beads. G' and G'' have similar features. The carboxylate beads detect the largest values of both G' and G'', followed in the descending order by the silica beads, the BSA PS beads, and the PEG beads. Both G' and G'' depend on probe size for all four bead surface properties, though for PEG beads G' has a very weak size dependence with the exception of the smallest bead size. For the slippery PEG beads, the smaller beads detect smaller moduli, hence, a positive slope is observed on the moduli vs. bead diameter plots. For the other three types of beads, the smaller beads detect larger moduli, resulting in a negative slope. The trend of measured moduli vs.

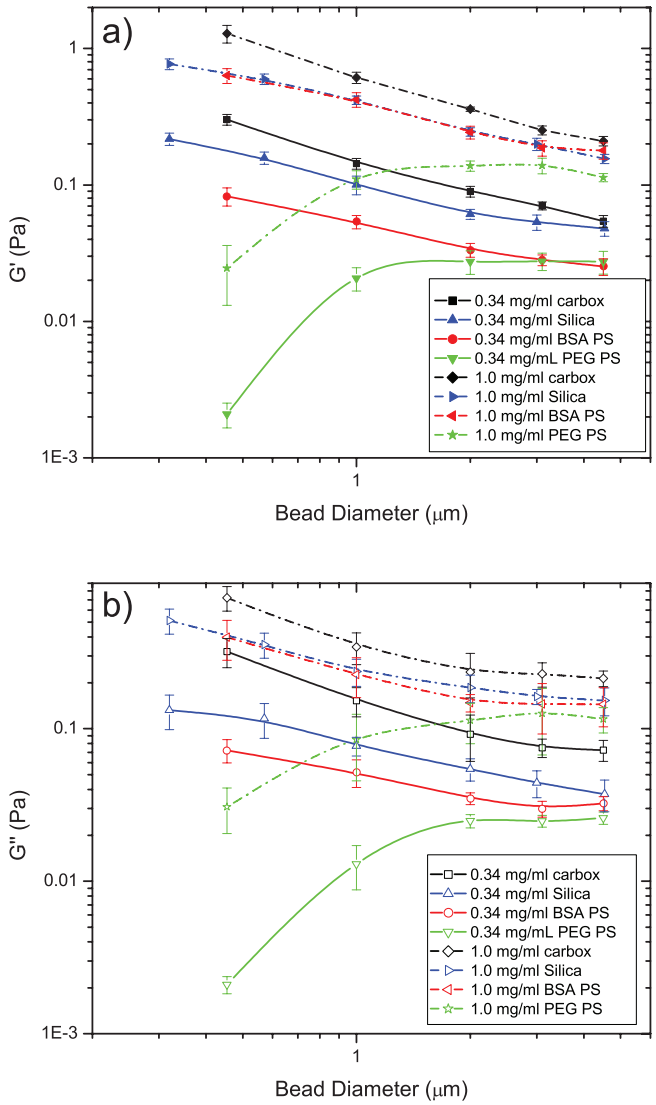

Figure 7: The storage (a, solid symbols) and loss (b, open symbols) moduli at 1.0 rad/sec are plotted as functions of bead diameter for two actin concentrations, 0.34 mg/ml (dash lines) and 1.0 mg/ml (solid lines).

probe diameter is reversed from the scaled MSDs, since shear moduli are proportional to the inverse of Fourier transformation of scaled MSD (Eq. 1). The reported shear moduli among all four types of beads tend to become parallel and get closer with increasing bead size or actin concentration. This behavior suggests that the surface effect becomes less important when either parameter increases, but the mechanisms may differ and are discussed in more detail later.

Our assessment of surface "stickiness" based on microrheology data proves to be consistent with direct imaging using fluorescent tags. In certain cases the former has proven even more

sensitive, evidenced by the difference it shows between the BSA and PEG beads. The consistency of both techniques also suggests the usefulness of microrheology for determining probe-network interactions under situations where direct imaging might not be feasible, or might not offer a clear answer due to limited optical resolution, etc.

IV. Discussion

Particle tracking microrheology is an effective tool to probe the viscoelastic properties of a wide range of soft materials including polymeric materials, biomaterials, and cells. However, complications like probe size dependence, probe surface chemistry, depletion effect and sample inhomogeneity impair the precise interpretation of microrheological data. Following up on the previous experiments that characterize the effects of probe surface chemistry on particle tracking microrheology [38, 39], we focus this study on the probe size dependency of the measured shear moduli, and correlate this with different surface properties. We advance the subject in two main aspects. First, we use quantitative confocal image analysis to characterize filament adsorption and depletion by selected types of probe bead surfaces. Second, through a systematic comparison of the diffusion of different sized beads in actin networks with four types of bead surfaces, we identified opposite trends of probe size dependence in microrheology between slippery and sticky beads. We were able to quantitatively characterize the probe size dependence of the measured moduli, and correlate the opposite trends with the bead surface being sticky or slippery. Qualitatively, probe size dependence of slippery beads can be explained by smaller beads hopping between network cages, thus underestimating the shear moduli. This can be avoided by choosing a probe size several times that of the network mesh size. For example, the probe size dependence for larger PEG beads is very weak, as shown in Fig. 7. The ensuing discussion focuses on models that help explain the size dependence that is not accounted for by the hoping effect.

Empirical models for probe size dependent microrheology detected by sticky particles

The probe size dependent microrheology of sticky particles is mainly caused by adsorption of actin filaments to the probe beads. This effect rearranges the spatial distribution of the

nearby filaments, and the influence of this rearrangement on microrheology depends on probe size. Here, we test two simple models to help understand the phenomena. Model I (scaling model) assumes that the MSD still follows a general scaling relation with the probe diameter, similar to the GSE relation, but with an exponent not necessarily equal to -1, namely,

$$\left\langle \Delta r^2 \right\rangle \sim R_0^{\mu}, \tag{4}$$

where R_0 is the probe particle radius. The fitting results of the exponents are shown in Table II. Rearranging terms of the GSE relation, we have $\langle \Delta r^2 \rangle \sim R_0^{-1} G^{-1}$. According to Hinner *et al.* [48], shear modulus $G \sim C_a^{1.4}$, hence, we obtain $\langle \Delta r^2 \rangle \sim R_0^{-1} C_a^{-1.4}$. Combining this expression with Eq. 4, we obtain $C_a \sim R_0^{-\frac{\mu+1}{1.4}}$, where C_a can be considered as effective actin concentration the bead probes in its proximity, and $-(\frac{\mu+1}{1.4})$ is the effective scaling exponent. For example, for 0.34 mg/ml actin solution, this effective exponent is 0.26, -0.29, -0.37 and -0.51, respectively, calculated for PEG, BSA, silica, and carboxylate beads from Table II. This simple scaling model provides us information about the change of actin filaments density detected by probe particles due to different surface properties. Note that this model appears applicable even for the slippery PEG, albeit with a positive exponent obtained from fitting.

Model II (non-scaling model) is based on the observation that as filaments stick to the bead surface, they extend out into the surrounding network (e.g. Fig. 3a and b), or the bead surface is packed with actin filaments (typically short ones), effectively increasing the size of probe particle. It may also be viewed as an alternative way of treating effective increase in local actin concentration. Here, we consider the semiflexible actin filaments as rigid rods, all the rods of the average filament length, and the attachment of the rods to the probe particle occurring at the center of each rod (Fig. 8a). This simplified model yields the MSD of beads as

$$\left\langle \Delta r^2 \right\rangle \sim R_{eff} = ((L/2)^2 + R_0^2)^{-1/2}, \tag{5}$$

where R_{eff} is effective probe radius and L is the average filament length. There are serious weaknesses in this model besides the simplifications specified above. For instance, it assumes that the filaments adsorbed on the beads surface do not entangle with the network. In reality, the entanglement length is on the order of $1\mu m$ for 0.34 mg/ml F-actin, comparable to the

		Model I	Model II
C_a (g/L)	Bead type	Exponent	Filament length
0.34	PEG	-1.36±0.03	N.A.
0.34	BSA	-0.60±0.04	1.56±0.36
0.34	silica	-0.48±0.04	1.89±0.29
0.34	carbox.	-0.28±0.08	4.48±0.40
1.0	PEG	-1.30±0.01	N.A.
1.0	BSA	-0.44±0.04	2.76±0.86
1.0	silica	-0.46±0.03	3.01±0.58
1.0	carbox.	-0.29±0.06	4.51±0.31

Table III: Summary of the model fitting and model comparison for eight different MSD vs. bead diameter curves (four different probe types and two actin concentrations) in Fig. 6.

thickness of the filaments stuck at the most adhesive carboxylate beads [9]. The adsorbed filaments might be integrated with the surrounding network so that the bead size rescaling scheme may no longer be valid.

Based on Model II, probe size dependency can be partly corrected. The complex shear modulus can be rewritten by substituting R_{eff} into Eq. 1 as $G^*(\omega) = \frac{k_B T}{\pi i \omega \sqrt{(\langle L \rangle/2)^2 + R_0^2 \mathcal{F}\{\langle \Delta r^2(t) \rangle\}}}$. Using this formula, we calculate a new set of storage and loss shear moduli for 0.34 mg/ml actin solution, plotted in comparison with the moduli calculated using the original GSE relation (Fig. 8b and c). For the model corrected storage moduli, the probe size dependence is almost removed, especially for the most sticky carboxylated bead. For the less sticky BSA bead, the model appears to over correct the size dependence. Also, there are some "over correction" for the loss moduli. This discrepancy is not so surprising since the simple assumption of our model implies extremely strong adhesion. We fit both models to all data sets in Fig. 6 with results shown in Table III. Note that none of these models address the depletion effect, the possible consequence of which on probe size dependence is discussed below.

Depletion effect

Depletion of actin filaments near the probe bead surface may also affect the application of particle tracking microrheology. This effect prevents the filaments from penetrating the particle surface, thus creating a layer of lower filament density in the adjacent region of

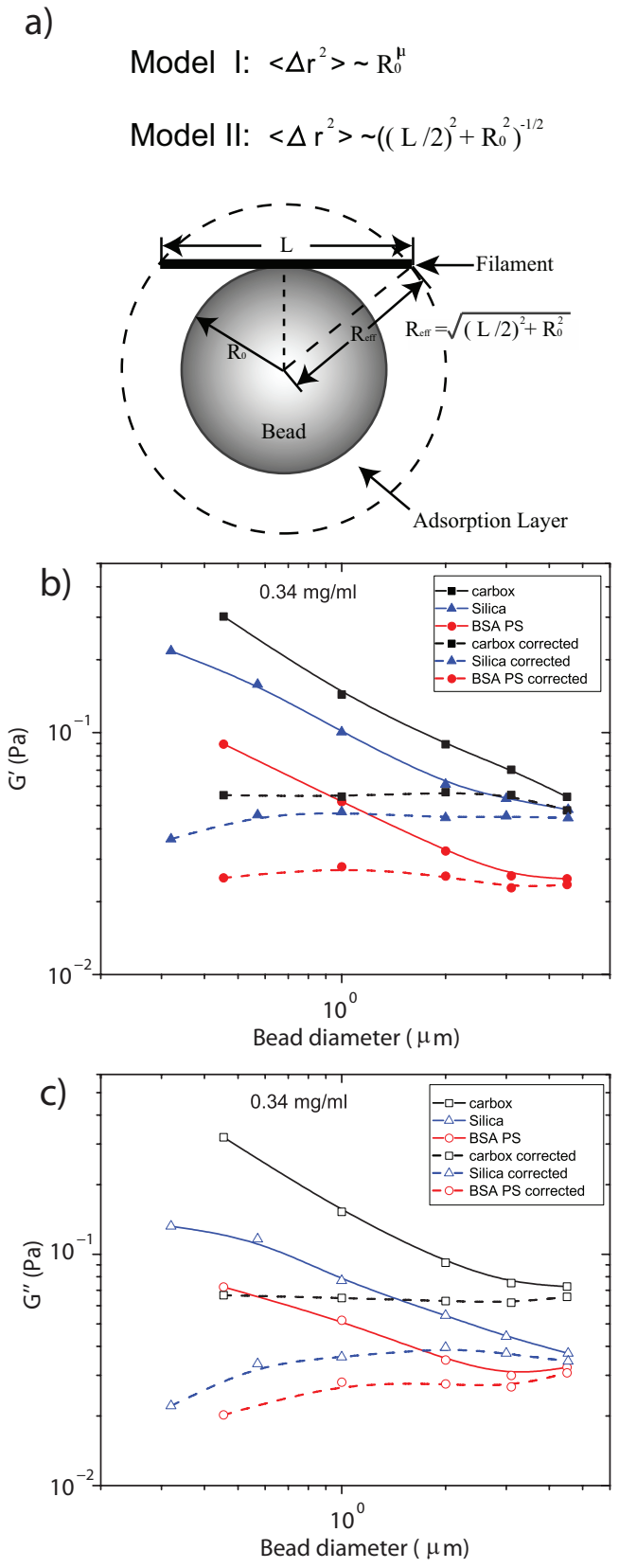

Figure 8: (Color online) Schematic illustration of Model II and moduli correction. (a) The empirical model assumes filaments to be rigid rods with an average filament length, and the attachment point of the rod to the probe particle is assumed to be at the center. (b) and (c): The storage and loss moduli after correction using Model II are shown as functions of bead diameter for 0.34 mg/ml actin solution in comparison with the data prior to the correction. Average filament length L is obtained from fitting and listed in Table III.

particles, possibly leading to underestimates of viscoelastic moduli. The depletion layer thickness varies with both the bead size and the lengths of the surrounding filaments, which are highly polydisperse in the case of F-actin [49]. Based on geometrical consideration, one may expect the depletion effect to be weak for bead size smaller than or comparable to the mesh size of the network, and stronger for larger bead. Thus, the measured shear moduli may be expected to decrease with increasing bead size. Judging from the weak probe size dependence of larger PEG beads, however, we conclude that depletion has only a secondary effect on microrheology measurements, compared with cage hopping or filament adsorption.

We note in the result section a discrepancy by a factor of 3 to 4 in the measured depletion layer thickness between what we obtained through confocal imaging and what was determined previously by Diffusing Wave Spectroscopy [45, 46]. This raises concern of the reliability of both techniques. We find a depletion layer around the 4.5 μm diameter adsorption resistant beads to be about 0.3 μm in thickness, by analyzing azimuthally averaged fluorescence profile of confocal images of Rhodamine BSA coated beads in the network of labeled actin at the concentration of 0.34 mg/ml. This measured thickness of depletion layer is consistent with those acquired using the same technique by Fisher and Kuo [41]. The criterion we adopted in defining the thickness of the depletion layer is somewhat empirical, and may be subject to correction. For instance, looking at the actin intensity profile shown in Fig. 3g and h, one might fit the profile to an exponential function such as $I\ [1 - \exp(-(r - R_0)/d)]$, where I is the fluorescence intensity of the bulk actin network, r is the radial position from the bead center, R_0 is the bead radius, and the decay constant d is the depletion layer thickness. Using this criterion, one would obtain a slightly larger layer thickness (0.4-0.5 μm). This higher estimate is still significantly lower than that obtained by Huh and Furst [45, 46], which is over 1 μm. We note, however, that the length in comparison from these references is obtained as the shell thickness following the theoretical model of Levine and Lubensky [50]. The calculation of the shell thickness required values of the bulk shear moduli at high frequencies, which were acquired indirectly by extrapolating the values measured in the lower frequencies with the assumption of a $G^* \backsim \omega^{3/4}$ scaling behavior. It is also pointed out by Huh and Furst that the shell thickness they obtained is larger by 50-90% than the so-called "nonlocality length" predicted by the PRISM theory [46, 51]. Clearly, the exact value of the depletion layer thickness is somewhat model dependent. Despite the different assumptions required for these distinct treatments, we confirm

that the depletion effect manifests itself in probing actin network rheology using micro-sized beads. Importantly, the thickness of the depletion layer is found to range from a few tenths of μm to about 1 μm for micro-sized probe beads in actin networks of comparable mesh size.

V. Concluding Remarks

One important insight from this study is the possibility that the size dependence of microrheology might be eliminated by choosing the right bead size and surface coating. A striking feature of the measured shear moduli (Fig. 7) is that the measured moduli as functions of probe diameter tend to become parallel and closer as the bead diameter increases, regardless of the bead type. Thus, to reduce the effect of probe surface chemistry, one needs to choose beads big enough to probe actin solutions. Ideally, probe diameter should be several times larger than the network mesh size. To reduce the probe size dependence, the optimal probe appears to be the non-sticky PEG grafted beads. In addition, it has been suggested that shorter PEG chains covering the beads with a high surface density would be more desirable than longer ones for the coating [39], in order to avoid patchy grafts that might complicate the surface properties of the probe. Our measurements using PEG grafted beads of a range of sizes suggest a new insight somewhat different from what has been recognized in the earlier study of Valentine *et al.* [39]. As shown in Fig. 7, the shear moduli measured by the PEG coated beads show very little size dependence for beads larger than the mesh size. This finding implies that as long as the probe beads used are significantly larger than the mesh size of the network, the bead surface can be totally slippery while serving as the ideal probe for network rheology. Some extent of stickiness is required for probing the network mechanics only as the slippery beads are smaller than the mesh size and tend to hop over cages in the network, thus not fully coupled with the network.

This study provides a cautionary but positive implication on applying particle tracking microrheology to measurement within live cells and tissues. On one hand, it is necessary to discern the size of the probe particle and all the macromolecular structures to which the probe might be attached, which often proves to be a challenging task. On the other hand, since the cellular environment is crowded with proteins, polymers and other soluble molecules, including those that account for the viscoelasticity to be probed, values acquired

by measuring the MSD of single probe particles are expected to be less sensitive to the bead surface physisorption than the measurements performed in low protein concentration networks, such as the one illustrated in this study. The mechanical properties probed by particle tracking may be highly variable among different cell types and within different regions of the cell because the cellular environment is mechanically diverse and extremely inhomogeneous. For this very reason, particle tracking microrheology remains a versatile technique for detecting local mechanical properties of living cells and other biological matrices, as well as non-biological soft materials.

Acknowledgments

We appreciate the helpful advice on beads coating from Profs. M. Valentine (UCSB) and M. Gardel (Univ. of Chicago). We also thank Dr. Henry Fu and Prof. Tom Powers for insightful discussions. We acknowledge funding by the National Science Foundation (CMMI 0825873).

---

[1] B. Alberts, D. Bray, J. Lewis, and et al., *Molecular biology of the cell* (Garland, New York, 2002).

[2] K. C. Holmes, D. Popp, W. Gebhard, and W. Kabsch, Nature **347**, 44 (1990).

[3] H. Isambert, P. Vernier, A. Maggs, A. Fattoum, R. Kassab, D. Pantaloni, and M. F. Carlier, J. Biol. Chem. **270**, 11437 (1995).

[4] F. Gittes, B. Mickey, J. Nettleton, and J. Howard, J. Cell Biol. **120**, 923 (1993).

[5] P. A. Janmey, S. Hvidt, J. Peetermans, J. Lamb, J. D. Ferry, and T. P. Stossel, Biochemistry **27**, 8218ÍC8227 (1988).

[6] P. A. Janmey, S. Hvidt, J. Kas, D. Lerche, A. Maggs, E. Sackmann, M. Schliwa, and T. P. Stossel, J. Biol. Chem. **269**, 32503 (1994).

[7] T. G. Mason, T. Gisler, K. Kroy, E. Frey, and D. A. Weitz, J. Rheol. **44(4)**, 917 (2000).

[8] F. Nakamura, E. Osborn, P. A. Janmey, and T. P. Stossel, J. Biol. Chem. **277**, 9148 (2002).

[9] M. L. Gardel, M. Valentine, J. C. Crocker, A. R. Bausch, and D. A. Weitz, Phys. Rev. Lett. **91**, 158302 (2003).

[10] I.Y.Wong, M. L. Gardel, D. R. Reichman, E. R.Weeks, M. Valentine, A. R. Bausch, and D. A.Weitz, Phys. Rev. Lett. **92**, 178101 (2004).

[11] J. He, M. Mak, Y. Liu, and J. X. Tang, Phys. Rev. E **78**, 011908 (2008).

[12] M. L. Gardel, J. H. Shin, F. C. MacKintosh, L. Mahadevan, P. Matsudaira, and D. A. Weitz, Science **304**, 1301 (2004).

[13] M. L. Gardel, F. Nakamura, J. H. Hartwig, J. C. Crocker, T. P. Stossel, and D. A. Weitz, Phys. Rev. Lett. **103**, 1762ÍC1767 (2006).

[14] J. Xu, J. F. Casella, and T. D. Pollard, Cell Motil. Cytoskeleton **42**, 73 (1999).

[15] A. B. Mathur, A. M. Collinsworth, W. M. Reichert, W. E. Kraus, and G. A. Truskey, J. Biomech. **34**, 1545 (2001).
[16] P. A. Janmey, S. Hvidt, J. Lamb, and T. P. Stossel, Nature **345**, 89 (1990).
[17] D. Mizuno, C. Tardin, C. F. Schmidt, and F. C. MacKintosh, Science **315**, 370 (2007).
[18] O. Lieleg, M. M. A. E. Claessens, Y. Luan, and A. R. Bausch, Phys. Rev. Lett. **101**, 108101 (2008).
[19] T. G. Mason, K. Ganesan, J. H. van Zanten, D. Wirtz, and S. C. Kuo, Phys. Rev. Lett. **79**, 3282 (1997).
[20] T. Gisler and D. A. Weitz, Phys. Rev. Lett. **82**, 1606 (1999).
[21] F. C. MacKintosh and C. F. Schmidt, Curr. Opin. Colloid In. **4**, 300 (1999).
[22] A. J. Levine and T. C. Lubensky, Phys. Rev. Lett. **85**, 1774 (2000).
[23] J. C. Crocker, M. T. Valentine, E. R. Weeks, T. Gisler, P. D. Kaplan, A. G. Yodh, and D. A. Weitz., Phys. Rev. Lett. **85**, 888 (2000).
[24] A. C. Lau, B. D. Hoffman, A. Davies, J. C. Crocker, and T. C. Lubensky, Phys. Rev. Lett. **91**, 198101 (2003).
[25] J. C. Crocker and B. D. Hoffman, Methods in cell biology **83**, 141 (2007).
[26] B. Schnurr, F. Gittes, F. C. MacKintosh, and C. F. Schmidt, macromolecules **30**, 7781 (1997).
[27] F. Gittes, B. Schnurr, P. D. Olmsted, F. C. MacKintosh, and C. F. Schmidt, Phys. Rev. Lett. **79**, 3286 (1997).
[28] J. Xu, A. Palmer, and D. Wirtz, Macromolecules **31**, 6486 (1998).
[29] A. Palmer, J. Xu, and D. Wirtz, Rheol. Acta **37**, 97 (1998).
[30] K. M. Addas, C. F. Schmidt, and J. X. Tang, Phys. Rev. E **70**, 021503 (2004).
[31] M. Valentine, L. Dewalt, and H. Ou-Yang, Journal of Physics: Condensed Matter **8**, 9477 (1996).
[32] R. R. Brau, J. M. Ferrer, H. Lee, C. E. Castro, B. K. Tam, P. B. Tarsa, P. Matsudaira, M. C. Boyce, R. D. Kamm, and M. J. Lang, J. Opt. A: Pure Appl. Opt. **9**, S103 (2007).
[33] F. Ziemann, J. Rädler, and E. Sackmann, Biophys. J. **66**, 2210 (1994).
[34] F. Amblard, A. C. Maggs, B. Yurke, A. N. Pargellis, and S. Leibler, Phys. Rev. Lett. **77**, 4470 (1996).
[35] T. P. Kole, Y. Tseng, and D. Wirtz, Methods Cell Biol. **78**, 45 (2004).
[36] J. Liu, M. L. Gardel, K. Kroy, E. Frey, B. D. Hoffman, J. C. Crocker, A. R. Bausch, and D. A. Weitz, Phys. Rev. Lett. **96**, 118104 (2006).
[37] A. C. Maggs, Phys. Rev. E **57**, 2091 (1998).
[38] J. L. McGrath, J. H. Hartwig, and S. C. Kuo, Biophys. J. **79**, 3258 (2000).
[39] M. T. Valentine, Z. E. Perlman, M. L. Gardel, J. H. Shin, P. Matsudaira, T. J. Mitchison, and D. A. Weitz, Biophys. J. **86**, 4004 (2004).
[40] J. D. Pardee and J. A. Spudich, Methods Cell Biol. **24**, 271 (1982).
[41] C. I. Fisher and S. C. Kuo, Proc. Natl. Acad. Sci. USA **106**, 133 (2009).
[42] T. G. Mason and D. A. Weitz, Phys. Rev. Lett. **74**, 1250 (1995).
[43] T. G. Mason, Rheol. Acta **39**, 371 (2000).
[44] D. Mizuno, D. A. Head, F. C. MacKintosh, and C. F. Schmidt, Macromolecules **41**, 7194 (2008).
[45] B. S. Chae and E. M. Furst, Langmuir **21**, 3084ÍC3089 (2005).
[46] J. Y. Huh and E. M. Furst, Phys. Rev. E **74**, 031802 (2006).
[47] C. F. Schmidt, M. Barmann, G. Isenberg, and E. Sackmann, Macromolecules **22**, 3638 (1989).
[48] B. Hinner, M. Tempel, E. Sackmann, K. Kroy, and E. Frey, Phys. Rev. Lett. **81**, 2614 (1998).

[49] P. A. Janmey, J. Peetermans, K. S. Zaner, T. P. Stossel, and T. Tanaka, J. Biol. Chem. **261**, 8357 (1986).
[50] A. J. Levine and T. C. Lubensky, Phys. Rev. E **63**, 041510 (2001).
[51] Y. L. Chen and K. S. Schweizer, J. Phys. Chem. B **108**, 6687 (2004).